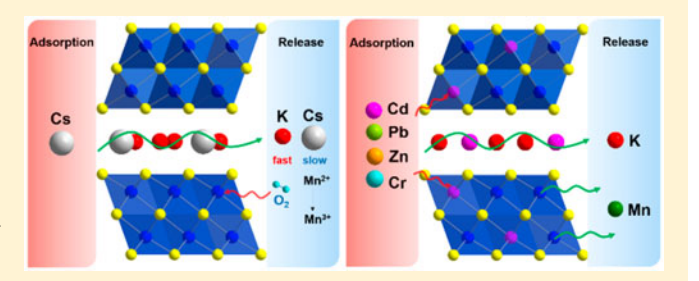
$K_x[Bi_{4-x}Mn_xS_6]$, Design of a Highly Selective Ion Exchange Material and Direct Gap 2D Semiconductor

Ruiqi Wang,[†] Haijie Chen,[‡] Yi Xiao,[†] Ido Hadar,[‡] Kejun Bu,[§] Xian Zhang, ^{||} Jie Pan,[§] Yuhao Gu,[†] Zhongnan Guo, Fuqiang Huang, **, and Mercouri G. Kanatzidis **

Supporting Information

ABSTRACT: Layered sulfides with high selectivity for binding heavy metal ions and radionuclide ions are promising materials in effluent treatment and water purification. Here we present a rationally designed layered sulfide K_x[Bi_{4-x}Mn_xS₆] (x = 1.28) deriving from the Bi₂Se₃-structure type by targeted substitution to generate quintuple $[Bi_{4-x}Mn_xS_6]^{x-}$ layers and K⁺ cations between them. The material has dual functionality: it is an attractive semiconductor with a bandgap of 1.40 eV and also an environmental remediation ion-exchange material. The compound is paramagnetic, and optical adsorption



spectroscopy and DFT electronic structure calculations reveal that it possesses a direct band gap and a work function of $\overline{5.26}$ eV. The K⁺ ions exchange readily with alkali or alkaline-earth ions (\overline{Rb}^+ , Cs^+ , and Sr^{2+}) or soft ions (Pb^{2+} , Cd^{2+} , Cr^{3+} , and Zn²⁺). Furthermore, when the K⁺ ions are depleted the Mn²⁺ ions in the Bi₂Se₃-type slabs can also be replaced by soft ions, achieving large adsorption capacities. The ion exchange reactions of $K_x[Bi_{4-x}Mn_xS_6]$ can be used to create new materials of the type $M_x[Bi_{4-x}Mn_xS_6]$ in a low temperature kinetically controlled manner with significantly different electronic structures. The $K_x[Bi_{4-x}Mn_xS_6]$ (x = 1.28) exhibits efficient capture of Cd²⁺ and Pb²⁺ ions with high distribution coefficient, K_d (10⁷ mL/g), and exchange capacities of 221.2 and 342.4 mg/g, respectively. The material exhibits excellent capacities even in high concentration of competitive ions and over a broad pH range (2.5-11.0). The results highlight the promise of the $K_x[Bi_{4-y}Mn_yS_6]$ (x = 1.28) phase to serve not only as a highly selective adsorbent for industrial and nuclear wastewater but also as a magnetic 2D semiconductor for optoelectronic applications.

■ INTRODUCTION

Effluent treatment of industrial and nuclear wastes has been a major concern around the world. 1-3 Several heavy metal ions (Pb²⁺, Cd²⁺, Hg²⁺, etc.) and radionuclides (¹³⁷Cs and ⁹⁰Sr, etc.) are major pollutants in these effluents and threaten human health and the environment. 4,5 Traditional commonly used and inexpensive adsorbents are clays, zeolites, and activated carbon.⁶⁻⁹ However, because of their weak binding affinity toward these hazardous metal ions, they suffer from relatively low selectivity and capacity, often cannot reduce the concentrations to desirable levels and tend to perform poorly in acidic conditions or in solutions with high salt concentration. 10-18

Recently, layered chalcogenides with ion-exchange properties have been demonstrated as promising adsorbents in a wide pH range. 19-35 The ability of the layered structure to expand along the stacking axis contributes to the fast ion exchange kinetics. One example is the KMS series compounds which are based on SnS_2 -type layers with mix-occupied Sn/M (M = Mn, Mg, In) sites and K⁺ intercalated between the layers. Their efficient adsorption properties have been confirmed on many heavy metal ions and radionuclides. 19-25,27,29,34-38 The high selectivity of these ion exchangers arises from their Lewis soft S² ligands in the anionic slabs, as the pollutant metal ions are soft Lewis acids. Hard ions such as H+, Na+ and Ca2+ only interact weakly with S^{2-} , thus the pollutant metal adsorption can be effective over a broad pH range and in the present of high salt concentration. 10,11 From this point of view, softer Lewis basicity in the chalcogenide slabs will benefit efficiency and selectivity in the heavy metal adsorption.

The Lewis basicity of the chalcogenide slab is determined mainly by the metal ion in the framework. Compared with Sn⁴⁺ in the KMS series, Bi³⁺ is less positively charged and possesses

Received: August 11, 2019 Published: September 30, 2019



[†]Beijing National Laboratory for Molecular Sciences and State Key Laboratory of Rare Earth Materials Chemistry and Applications, College of Chemistry and Molecular Engineering, Peking University, Beijing 100871, P. R. China

Department of Chemistry, Northwestern University, 2145 Sheridan Road, Evanston, Illinois 60208, United States

[§]CAS Key Laboratory of Materials for Energy Conversion and State Key Laboratory of High-Performance Ceramics and Superfine Microstructure, Shanghai Institute of Ceramics, Chinese Academy of Sciences, Shanghai 200050, P. R. China

^{||}Qian Xuesen Laboratory of Space Technology, China Academy of Space Technology, Beijing 100094, P. R. China

larger ion radii, thus we can expect that the Bi³+-based slabs are more Lewis basic and should possess stronger binding affinity toward heavy metal ions. The five-atom-thick Bi₂Se₃-type layers are an ideal kind of matrix for the rational design of new ion exchangers. This is done by replacing a fraction of Bi³+ ions in the structure with other metal ions of lower positive charge. This creates a negatively charged layer whose exact charge depends on the M metal such as $\left[\text{Bi}_{2-x}\text{M}_x\text{Se}_3\right]^{\delta-}$. The compounds $\text{A}_x\text{Cd}_x\text{Bi}_{4-x}\text{Q}_6$ (A = K, Rb, Cs; Q = S, Se), are examples of this process, 39,40 however, these materials contain heavy and toxic Cd²+ which limits their application in effluent treatment.

In this work, we targeted the $K_x[Bi_{4-x}Mn_xS_6]$ with several considerations in mind. First, the presence of Mn makes the system suitable for environmental remediation investigations. Second, the relatively weak Mn-S bonds imply that Mn²⁺ can also contribute to the adsorption capacity of heavy metal ions. The solubility constant $k_{\rm sp}$ of MnS (4.65×10^{-14}) is more than 10 orders of magnitude higher than those of heavy metal sulfides such as CdS (8.0×10^{-27}) and PbS (7.0×10^{-29}) . 41–43 The Mn contribution of adsorption capacity has been demonstrated in KMS-1 ($K_{2x}Mn_xSn_{3-x}S_6$ (x = 0.5-0.95) and $K_{2x}Mn_{1-x}PS_3$, as Mn^{2+} of MnS_6 octahedral units inside the layers can be exchanged by Cd^{2+} and Pb^{2+} . Third, the variable valence states Mn can adopt in the structure can provide an additional knob to further tune the ion-exchange function as well as the magnetic properties. We hypothesized that the five-atom-thick octahedral Bi₂Se₃-type slab could be a better host for achieving this function than the three-atomthick SnS₂-type KMS-1 slabs because Mn²⁺ can be better protected from oxidation inside the thicker slabs.

Guided by the above-mentioned concepts, we synthesized $K_x[Bi_{4-x}Mn_xS_6]$ (x = 1.28) (i.e., $K_{1.28}Mn_{1.28}Bi_{2.72}S_6$) with quintuple Bi_2Se_3 -type $[Bi_{4-x}Mn_xS_6]^{x-}$ layers and K^+ cations between them. Optical adsorption and DFT calculations reveal that it is a new semiconductor with a direct band gap of 1.40 eV, potentially promising for optoelectronic applications. This compound is paramagnetic and exhibits anisotropic and thermally activated charge transport behavior. Various M ions such as Rb⁺, Cs⁺, Sr²⁺, Pb²⁺, Cd²⁺, Cr³⁺, and Zn²⁺ replace the K⁺ ions rapidly and topotactically, and even the Mn²⁺ ions held in the slabs can be exchanged totally or partially by soft ions $(M^{2+} = Pb^{2+}, Cd^{2+}, Cr^{3+}, and Zn^{2+})$. These ion exchange reactions create new materials of the type $M_{\nu}[Bi_{4-x}Mn_{x}S_{6}]$ in a low temperature kinetically controlled manner with significantly different electronic structures as verified by optical absorption and work function measurements. With Cs⁺ exchange a remarkable topotactic oxidation of Mn²⁺ to Mn³⁺ was observed, and confirmed with single-crystal X-ray diffraction and X-ray photoelectron spectroscopy (XPS). We show highly selective absorption of Cd²⁺ and Pb²⁺ by $K_r[Bi_{4-r}Mn_rS_6]$ (x = 1.28) over a broad pH range that follows the Langmuir model with high exchange capacities of 221.2 and 342.4 mg/g and particularly high distribution coefficient K_d of 10^7 mL/g. The selectivity for heavy metal ion remediation, high pH resistance, and discrimination against hard Lewis acid ions make the $K_x[Bi_{4-x}Mn_xS_6]$ system promising for future industrial and nuclear waste applications.

EXPERIMENTAL SECTION

Reagents. The following reagents were used as-purchased: Mn (Alfa Aesar, 99.9%), Bi (Alfa Aesar, 99.9%) and S (Alfa Aesar, 99.9%).

 K_2S_5 was prepared by the stoichiometric reaction of elements in liquid NH $_3$ as previously described. ^{44,45}

Synthesis of K_x[Bi_{4-x}Mn_xS₆] (x = 1.28). All operations were carried out in an Ar-filled glovebox. 0.0592 g K₂S₅ (0.25 mmol), 0.0275 g Mn (0.5 mmol), 0.2299 g Bi (1.1 mmol), and 0.0368 g S (1.15 mmol) were mixed and loaded in a carbon coated silica tube with an inner diameter of 10 mm. The tube was flame-sealed under vacuum (10^{-3} mbar), heated to 700 °C in 10 h, held for 48 h, and followed by slow cooling to 450 °C in 3 days. Black single crystals were obtained with a yield of ~99% based on the Bi element. Large plate-like single crystals ($1 \times 2 \times 0.2 \text{ mm}^3$) of K_x[Bi_{4-x}Mn_xS₆] (x = 1.28) used for electrical resistivity measurement were synthesized by adding extra 0.0592 g K₂S₅ (0.25 mmol) into the combination of reactants (to act as a flux) and following the same heating procedure mentioned above. The product was washed with deionized water twice to remove the extra K₂S₅.

Single Crystal X-ray Crystallography. Single crystals were selected from the products and mounted on the tips of glass fiber loops with glue for X-ray diffraction. X-ray diffraction data were collected at 180 K on a Rigaku XtaALB PRO 007HF single crystal X-ray diffractometer equipped with mirror-monochromatized Mo-Kα radiation ($\lambda = 0.71073$ Å) and Oxford Cryo stream (80–500 K). The crystal structures were solved via direct methods and refined by full-matrix least-squares on F^2 using the SHELXTL program package. Multiscan absorption corrections were performed. The crystallographic data and structure refinement results of $K_x[Bi_{4-x}Mn_xS_6]$ (x = 1.28) are shown in Table 1 and the selected bond lengths and angles

Table 1. Crystallographic Data (180 K) and Details of the Structure Refinement of $K_x[Bi_{4-x}Mn_xS_6]^{a,b,c}$

formula	$K_{1.28}Mn_{1.28}Bi_{2.72}S_6$
space group	$P6_3/mmc$
$F_{\rm w} (g \cdot {\rm mol}^{-1})$	881.18
a (Å)	3.9521(2)
c (Å)	23.094(2)
$V(Å^3)$	312.38(3)
crystal color	black
$\rho_{\rm c} ({\rm g\cdot cm^{-3}})$	4.684
$\mu \text{ (mm}^{-1})$	40.828
F(000)	378
data/parameters	224/16
$R_{\rm int}$	0.0697
$R1[I > 2\sigma(I)]$	0.0238
wR_2 (all data)	0.0519
GOF	1.269

 ${}^{a}R = \Sigma ||F_{0}| - |F_{c}||/\Sigma |F_{0}|. \quad {}^{b}wR = \Sigma \{[w(|F_{0}|^{2} - |F_{c}|^{2})^{2}]/\Sigma [w(|F_{0}|^{4})]\}^{1/2}.$ ${}^{c}w = 1/[\sigma^{2}(F_{0}^{2}) + (0.0146P)^{2} + 3.0862P], \text{ where } P = (F_{0}^{2} + 2F_{c}^{2})/3$

are shown in Table 2. Atomic coordinates, equivalent isotropic displacement parameters, and anisotropic displacement parameters are shown in Tables S1 and S2 of the Supporting Information (SI).

Physical Properties Measurements. Direct-current magnetization measurements as a function of temperature and magnetic field were performed using a Physical Properties Measurement System (PPMS) from Quantum Design. Zero-field-cooled (ZFC) and field-cooled (FC) susceptibility data were collected from 300 to 2 K in an

Table 2. Selected Bond Lengths and Angles for $K_x[Bi_{4-x}Mn_xS_6]$ (x = 1.28)

bond type	distance (Å)	angle type	angle (deg)
$Bi-S1 \times 3$	2.8963(3)	$S1-Bi-S1 \times 3$	86.05(2)
$Bi-S2 \times 3$	2.674(2)	$S2-Bi-S2 \times 3$	95.30(8)
$K1-S2 \times 6$	3.456(2)	$S2-Bi-S1 \times 2$	89.14(4)
$K2-S2 \times 6$	3.456(2)	$S2-Bi-S1 \times 2$	89.14(4)

applied magnetic field of 1 T. Magnetic hysteresis, M(H), were collected with applied magnetic field from -1 to 1 T at 2, 10, 50, 100, 150, 200, and 300 K, respectively. Electrical resistivity measurements on single crystals were done using the standard two-probe method on the PPMS.

Work Function. The work function data were collected by photoemission yield spectroscopy in air (PYSA). In PYSA, the sample is scanned with monochromatic UV light (3.4–6.2 eV) and the generated photoelectrons are measured at each energy, the work function is defined by the onset in the PYSA spectrum. ⁴⁷ PYSA measurements were performed using an AC-2 spectrometer (Riken Keiki).

Electronic Structure Calculations. First-principles calculations were performed by using the Projected Augmented Wave Method $(PAW)^{48}$ within the density functional theory (DFT) as implemented in the Vienna Ab Initio Simulation Package $(VASP)^{49-51}$ The exchange correlation functional was treated within the spin-polarized generalized gradient approximation (GGA) and parametrized by Perdew—Burke—Ernzerhof (PBE) version. The cutoff energy of plane wave basis was set to 380 eV and the Monkhorst—Pack k-point grid of $4 \times 6 \times 3$ was used for Brillouin zone (BZ) sampling. The crystal structure and the lattice parameters were fixed as the values observed in experiments during the structural optimization, while the positions of atoms were relaxed until the atomic forces on each atom were less than 0.01 eV/Å.

ICP-AES and ICP-MS Analysis. The concentration of K^+ , Cs^+ , Mn^{2+} , Cd^{2+} , and Pb^{2+} in the range of 1–100 ppm were determined using a Leeman Prodigy 7 ICP-AES spectrometer. Standards of these ions were prepared by diluting the commercial \sim 1000 ppm ICP standards, and the calibration was liner with maximum errors of 5%. The solutions were diluted to appropriate concentrations using 1 wt % HNO₃. The intensity was obtained using a 35 s exposure, and the result was the average of three readings. The residual concentrations of Cd^{2+} and Pb^{2+} in the solutions after ion exchange were at ppb levels and were determined by ICP-MS using a PerkinElmer NexION 350X ICP-MS spectrometer.

lon-Exchange Experiments. The ion-exchange properties of $K_x[Bi_{4-x}Mn_xS_6]$ (x=1.28) were studied as follows: the crystals of the material (~10.0 mg) were added into 0.2 mol/L aqueous solutions (10 mL) of RbCl, CsCl, SrCl₂·6H₂O, CrCl₃·6H₂O, ZnCl₂, CdCl₂·2.5H₂O, or Pb(NO₃)₂, respectively. After 3 days, the products were collected by filtration, washed with water and acetone and then dried in air. Ion-exchange crystals were selected for SEM imaging and EDS analysis. Rb⁺, Cs⁺ and Zn²⁺-exchanged single crystals were picked out for detailed crystallographic analysis. Ground powder of $K_x[Bi_{4-x}Mn_xS_6]$ (x=1.28) (100 mg) were add in 0.2 mol/L aqueous solutions (20 mL) of the ions mentioned above. The mixture was stirred for 24 h and the solid products were collected by filtration and characterized with PXRD and UV—vis spectroscopy.

Sorption studies of $K_x[Bi_{4-x}Mn_xS_6]$ (x = 1.28) with Cs^+ , Cd^{2+} , and Pb^{2+} were carried out by the batch method at V:m = 1000 mL/g at RT. An amount of 10.0 mg ground powder of $K_x[Bi_{4-x}Mn_xS_6]$ (x = 1.28) was added into 10 mL aqueous solutions containing gradient concentration of Cs^+ , Cd^{2+} , or Pb^{2+} . The mixture was stirred for 24 h and then filtered. The concentration of ions was determined by ICP-AES or ICP-MS. The obtained data were used for the determination of the sorption isotherms.

Kinetic studies were carried out to estimate the rate and pathways of sorption. Typically, amounts of 10.0 mg of ground powder of $K_x[Bi_{4-x}Mn_xS_6]\ (x=1.28)$ were added into 10 mL of $Cs^+\ (100\ ppm)$, $Pb^{2+}\ (350\ ppm)$ or $Cd^{2+}\ (200\ ppm)$ aqueous solutions in individual tubes and stirred. After certain time intervals, the solutions were filtered, and the concentrations were determined by ICP-AES.

RESULTS AND DISCUSSION

Synthesis and Thermal Behavior. $K_x[Bi_{4-x}Mn_xS_6]$ (x = 1.28) was synthesized via solid state reactions of K_2S_5 , Mn, Bi, and S at 700 °C. The phase purity of the as-synthesized product was validated by comparing the experimental PXRD

pattern with the simulated one, as shown in Figure 1a. Energy dispersive X-ray spectroscopy (EDS) confirmed that all the

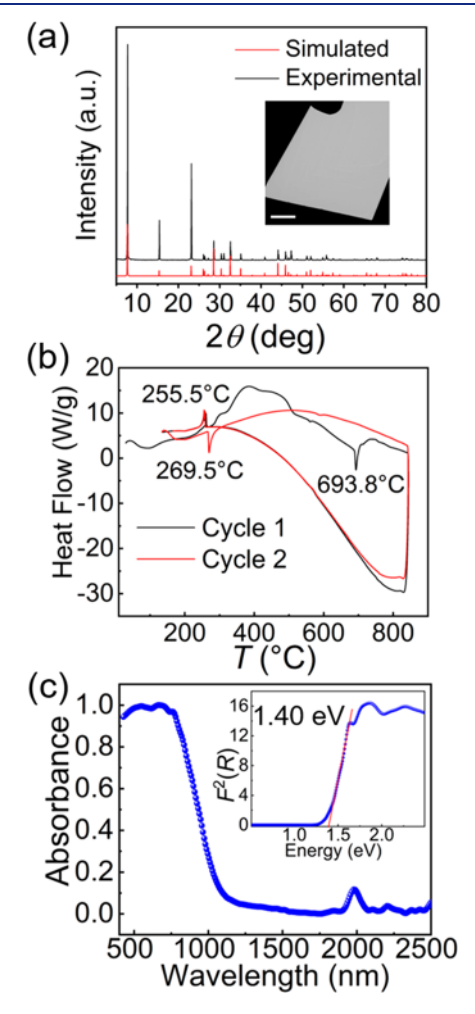


Figure 1. (a) Simulated (red) and experimental (black) PXRD patterns of $K_x[Bi_{4-x}Mn_xS_6]$ (x=1.28). Inset is the SEM image of single crystal. The scale bar is 10 μ m. (b) The DSC curve and (c) UV–vis diffuse reflectance spectroscopy of $K_x[Bi_{4-x}Mn_xS_6]$ (x=1.28), inset: Plot of $F^2(R)$ vs energy obtained using the Kubelka–Munk equation (see SI).

elements distribute uniformly in the crystals, as shown in Figure S1. The accurate molar ratio of K/Mn/Bi as determined by ICP-AES is 1.32/1.28/2.72 which is consistent with the single crystal X-ray crystallographic refinement. By adding extra reactant K₂S₅ to serve as flux, we succeeded in obtaining large flaky crystals $(1 \times 2 \times 0.2 \text{ mm}^3)$ suitable for the resistivity measurements. The thermal behavior of $K_x[Bi_{4-x}Mn_xS_6]$ (x =1.28) was investigated using DSC analysis. In the first heating cycle of the DSC a single endothermic peak was observed at 693.8 °C, and on cooling a single exothermic peak at 255.5 °C corresponding to the crystallization of Bi metal, Figure 1b. In the second cycle the endothermic peak at 693.8 °C disappeared, while a new peak appeared at 269.5 °C on heating, indicating the melting of Bi. The product obtained after DSC analysis was examined by PXRD, and the pattern can be well matched with the patterns of KBiS₂ (PDF#08-0441), MnS (PDF#06-0518), and Bi (PDF#44-1246), as shown in Figure S2. Therefore, $K_x[Bi_{4-x}Mn_xS_6]$ (x = 1.28) melts incongruently.

Crystal Structure. The structure and stoichiometry of $K_x[Bi_{4-x}Mn_xS_6]$ (x=1.28) was determined from the single crystal X-ray crystallographic refinements. The crystallographic data and structure refinements are summarized in Table 1. The structure derives from the layered quintuple hexagonal Bi_2Se_3 structure, with some Bi^{3+} sites in the slabs replaced by Mn^{2+} ions which requires disordered alkali cations between the interlayers to balance charge (Figure S3). This compound crystallizes in space group $P6_3/mmc$ and is isostructural with the compounds $Cs_{1.2}Ag_{0.6}Bi_{3.4}Q_6$ (Q=S, Se) and $A_xCd_xBi_{4-x}Q_6$ (A=K, Rb, Cs; Q=S, Se)

 $K_x[Bi_{4-x}Mn_xS_6]$ (x=1.28) is composed of anionic Bi_2Se_3 -type quintuple $[Bi_{2.72}Mn_{1.28}S_6]^{1.28-}$ layers of edge-sharing distorted $(Mn/Bi)S_6$ octahedra intercalated by K^+ cations, Figure 2a, b. There are two independent K sites (2b, 2c)

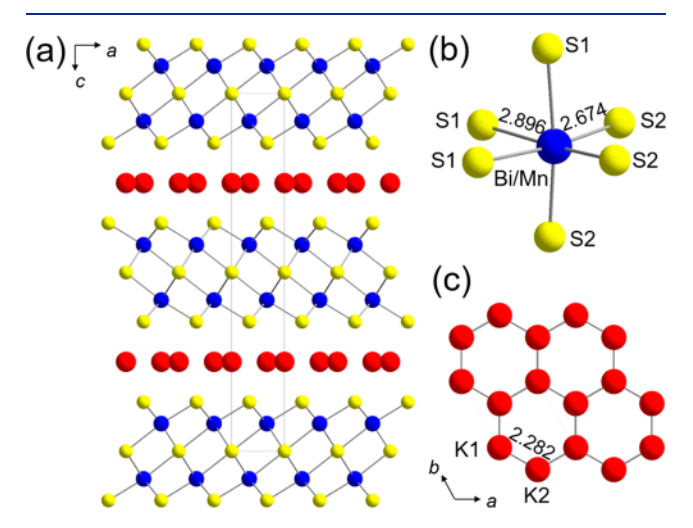


Figure 2. (a) Structure of $K_x[Bi_{4-x}Mn_xS_6]$ (x = 1.28) viewed down [010] with quintuple Bi_2Se_3 -type layers. (b) Coordination environments of the Bi/Mn site. (c) Graphene-like arrangement of the disordered K^+ layer viewed down [001].

Wyckoff position), one independent Bi/Mn site (4f, occupancy: Bi 68.0% and Mn 32.0%), and two independent S sites (2a, 4f). The coordination environment of (Mn/Bi)S₆ octahedral is shown in Figure 2b. The Mn²⁺ ion in the (Mn/Bi)S₆ octahedra of K_x[Bi_{4-x}Mn_xS₆] (x = 1.28) is in a relatively loose coordination environment originally intended for the Bi³⁺ atoms. The two K sites are partly occupied with refined occupancies 21% and 43%. A graphene-like layered arrangement of K⁺ is obtained after omitting the partial occupation of

K sites, as shown in Figure 2c. The open interlayer space of $K_x[Bi_{4-x}Mn_xS_6]$ and relatively large thermal factors of K^+ atoms (Tables S1 and S2) imply a strong tendency to engage in facile ion-exchange.

Optical Absorption and Electronic Structure Calcu**lations.** The optical absorption properties of $K_r[Bi_{4-r}Mn_rS_6]$ (x = 1.28) were investigated by UV-vis diffuse reflectance spectroscopy, which shows a well-defined band gap of 1.40 eV (Figure 1c). In order to gain insight into the nature of the electronic structure we performed DFT calculations using an ordered structure model with the space group Cmcm (Figure S4a) to represent the mixed-occupied Mn/Bi sites that is a periodic array of fully occupied Mn and Bi sites. The [Bi_{2.72}Mn_{1.28}S₆].¹²⁸⁻ layers were approximated as [Bi₄Mn₂S₉]²⁻ layers with the Mn:Bi ratio of 1:2. In each of the sublayers, every MnS₆ octahedron is surrounded by six BiS₆ octahedra, as shown in Figure S4b. The disordered K+ layers were modified by removing all 4c K sites and fully occupying the 8g K sites (Figure S4c). Charge neutrality was satisfied with a general formula of K2Bi4Mn2S9. Because of the presence of magnetic Mn²⁺ ions spin-polarized calculations were carried out. The electronic structures and density of states (DOS) of K₂Bi₄Mn₂S₉ are depicted in Figure 3. The valence band maximum (VBM) and the conduction band minimum (CBM) are both located at Γ point (Figure 3a), which indicates the direct-band gap character. The effective masses of the CBM (m_e^*) and VBM (m_h^*) for a and c directions were calculated by fitting the E-k bands around the CBM and VBM with m* =

 $\hbar^2 \left(\frac{\partial^2 E}{\partial k^2}\right)^{-1}$, where \hbar is Planck's constant, E is the band energy, and k is the wave vector. The calculated electron effective mass (m_e^*) and hole effective mass (m_h^*) along the a direction $(\Gamma - Y)$ is $0.36m_0$ and $1.17m_0$ $(m_0$ is the effective mass of free electron), respectively, while both m_e^* and m_h^* along the c direction $(\Gamma - Z)$ are essentially infinite. This points to the two-dimensional nature of the material and explains its highly anisotropic conductivity.

For $K_2Bi_4Mn_2S_9$ the DOS of two different spin directions are shown in Figures 3b and S5. The VBM is mainly contributed by S 3p states and Mn 3d states in the spin-up direction, while the VBM of the spin-down direction locates at -0.5 eV. The Bi 6s lone-pair states mainly locate between -1.5 eV and the VBM in both spin directions. The Bi 6p and S 3p states make similar contribution to the CBM in both spin directions, while the spin-down Mn 3d states also significantly contribute to the CBM. The spin-up Mn 3d states are fully occupied and mainly

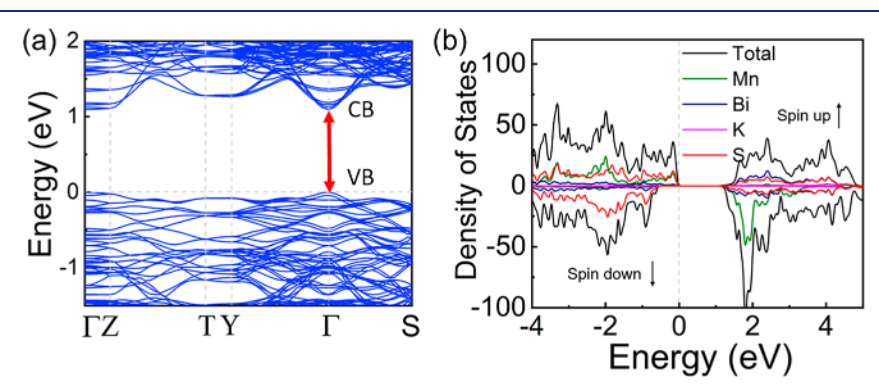


Figure 3. (a) Electronic band structure and direct gap between VB and CB. (b) Spin-polarized total and partial density of states (DOS) of $K_2Bi_4Mn_2S_9$.

locate between -4 and -1.3 eV, while the spin-down states are empty in the range of 1.2-2.7 eV. These results indicate that the $\mathrm{Mn^{2+}}$ ions in $\mathrm{MnS_6}$ octahedra are in high spin (HS) state, which implies the presence of the magnetic properties presented below.

Magnetic Properties. The magnetic properties, and specifically the magnetization (M) and inverse molar magnetic susceptibility $(1/\chi)$ of $K_x[Bi_{4-x}Mn_xS_6]$ (x=1.28) from 2 to 300 K are shown in Figure 4a. No magnetic transition was

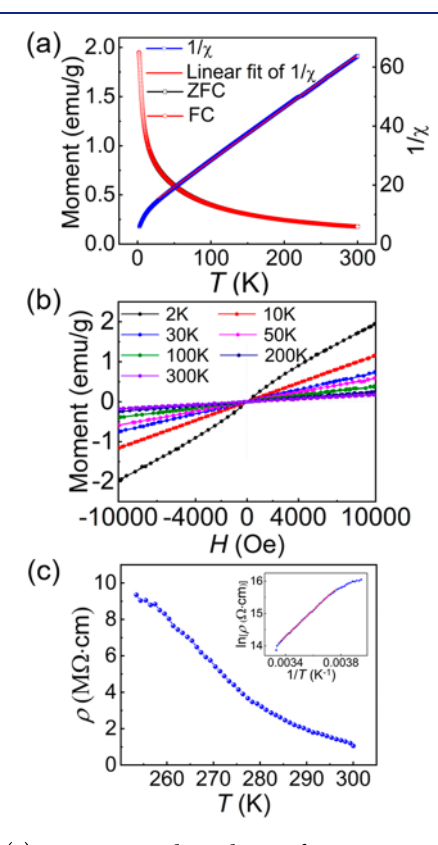


Figure 4. (a) Temperature dependence of magnetization (black and red dots) and inverse magnetic susceptibilities $(1/\chi)$ (blue dots), as measured at 1 T in the temperature range 2–300 K, the red lines are linear fit of the $1/\chi$ -T curves between 25 and 300 K; (b) M-H curves at 2, 10, 30, 50, 100, 200, and 300 K. (c) Electrical resistivity data as a function of temperature for a single crystal of $K_x[Bi_{4-x}Mn_xS_6]$ (x=1.28). The red line in the inset is a linear Arrhenius fitting for the temperature dependence of resistivity between 267 and 297 K ($E_a=0.35$ eV).

observed which indicates paramagnetic behavior of $K_x[Bi_{4-x}Mn_xS_6]$ (x=1.28). The $1/\chi-T$ curve can be well fitted by the Curie–Weiss law with Curie constant C=5.590 K emu/mol and Curie–Weiss temperature $\theta=-58.32$ K. The negative θ indicates relatively strong antiferromagnetic interactions between the Mn^{2+} ions. The effective magnetic moments of Mn^{2+} calculated from the Curie constants are $\mu_{\rm eff}=5.22~\mu_{\rm B}$, which is close to but somewhat smaller than the calculated 5.92 $\mu_{\rm B}$ of HS Mn^{2+} (d^5 , S=5/2). The data suggest that the Mn^{2+} ions in MnS_6 octahedra are in a high-spin state. The magnetization (M) as a function of the applied magnetic field (H) was measured between 2 and 300 K (Figure 4b), and the linear dependence of M-H curves also reveals the antiferromagnetic character of $K_x[Bi_{4-x}Mn_xS_6]$ (x=1.28).

Electrical Resistivity. The electrical resistivity measurements on single crystals are depicted in Figure 4c. The

resistivity versus temperature data exhibit thermally activated charge transport behavior where the resistivity increases rapidly with falling temperature. This confirms the semiconducting nature of the material. The Arrhenius dependence $\rho(T) = \rho_0$ $\exp(E_a/k_BT)$ (ρ_0 is a pre-exponential factor, E_a is the activation energy, and $k_{\rm B}$ is the Boltzmann constant) was used to describe the temperature dependence of resistivity (inset in Figure 4c). The E_a value was estimated to be 0.35 eV in the temperature range of 267-297 K. Two other classical models for semiconducting transport, the small polaron hopping (SPH) model (expressed as $\rho(T)/T \propto \exp(E_p/k_BT)$, E_p is activation energy)⁵³ and variable range hopping (VRH) (expressed as $\rho(T) \propto \exp(T_0/T)^1/^4 T_0$ is characteristic temperature)⁵⁴ were also used to fit the curve. These gave $E_p = 0.37$ eV in the SPH model and $T_0 = 235$ K in the VRH model (Figure S6), values of activation energy that likely represent defect states lying in the middle of the energy gap.

lon-Exchange Properties of $K_x[Bi_{4-x}Mn_xS_6]$ (x = 1.28) and the Creation of New Materials. The ion-exchange properties of $K_x[Bi_{4-x}Mn_xS_6]$ (x = 1.28) for Rb^+ , Cs^+ , Sr^{2+} , Cr^{3+} , Zn^{2+} , Cd^{2+} , and Pb^{2+} in aqueous solution are excellent. SEM and EDS analysis of the exchanged materials confirmed that all K^+ ions can be replaced by these ions, as depicted in Figures 5 and S7. Moreover, the Mn^{2+} ions in the semiconducting slabs can also be exchanged by the soft ions such as Cr^{3+} , Zn^{2+} , Cd^{2+} , and Pb^{2+} . Although the intralayer Mn^{2+} ion exchange has been reported in $K_{2x}Mn_xSn_{3-x}S_6$ (x = 0.5-0.95) (KMS-1), and $K_{2x}Mn_{1-x}PS_3$, the fact that we see

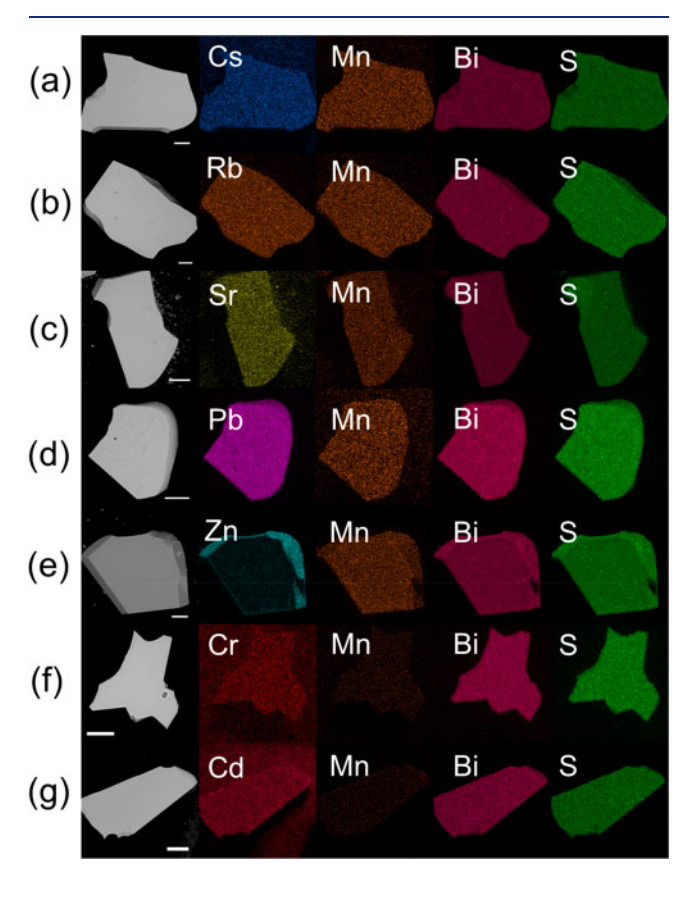


Figure 5. SEM images and EDS mapping analysis of (a) Cs⁺, (b) Rb⁺, (c) Sr²⁺, (d) Pb²⁺, (e) Zn²⁺, (f) Cr³⁺, and (g) Cd²⁺ exchanged products of $K_x[Bi_{4-x}Mn_xS_6]$ (x=1.28). The scale bars stand for 10 μ m.

Table 3. Element Ratios, Band Gaps, and Work Functions of $K_x[Bi_{4-x}Mn_xS_6]$ (x = 1.28) and Ion-Exchanged Powder Products

compounds	element ratio (ICP-AES)	band gap (eV)	work function (eV)
$K_{1.28}Mn_{1.28}Bi_{2.72}S_6$	K:Mn:Bi = 1.32:1.28:2.72	1.40	5.26
Zn ²⁺ -exchange product	Zn:Mn:Bi = 1.26:0.50:2.72	1.30	5.80
Cd ²⁺ -exchange product	Cd:Bi = 1.91:2.72	1.26	5.73
Pb ²⁺ -exchange product	Pb:Mn:Bi = 1.53:0.20:2.72	1.10	5.41

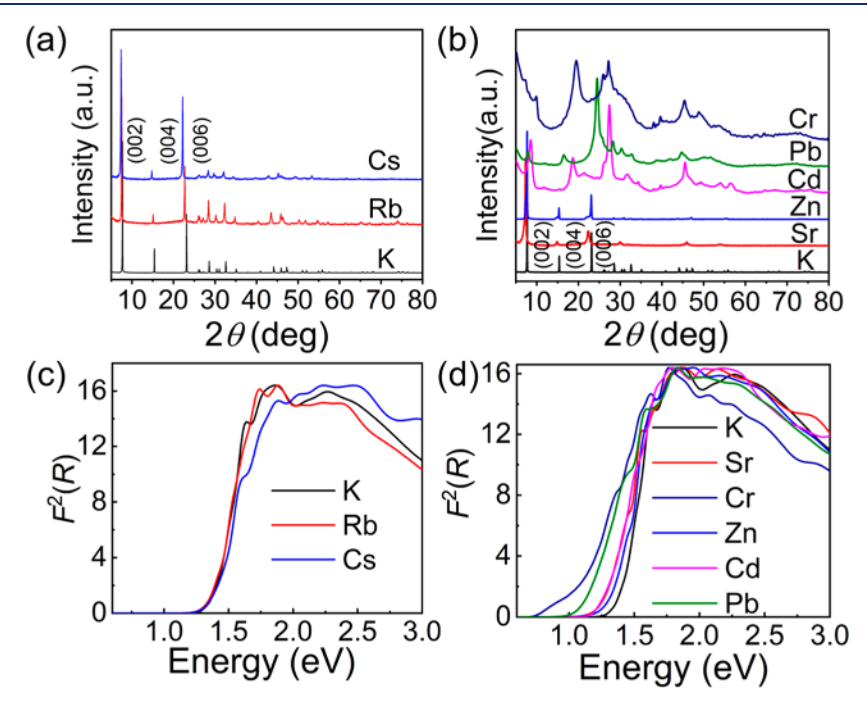


Figure 6. Normalized PXRD patterns of (a) Rb⁺ and Cs⁺ exchanged products and (b) Sr²⁺, Zn²⁺, Cd²⁺, Pb²⁺, and Cr³⁺ exchanged products; electronic absorption spectra and band gaps of the (c) Rb⁺ and Cs⁺ exchanged products and (d) Sr²⁺, Zn²⁺, Cd²⁺, Pb²⁺, and Cr³⁺ exchanged products.

again in $K_x[Bi_{4-x}Mn_xS_6]$ (x=1.28) suggests this process is more general. The average Mn/Bi–S bond length (2.750 Å) in $K_x[Bi_{4-x}Mn_xS_6]$ (x=1.28) is obviously longer than the Mn/Sn–S bond length (2.572 Å) in KMS-1, indicating a weaker Mn–S bond strength. Thus, we can expect that Mn²⁺ in $K_x[Bi_{4-x}Mn_xS_6]$ (x=1.28) can be easily exchanged with various soft ions.

For example, we observe that Cr^{3+} and Cd^{2+} can completely replace Mn^{2+} in the slabs, while in the case of Pb^{2+} some Mn^{2+} ions (\sim 16%) remain and distribute uniformly in the Pb^{2+} exchanged crystals (Figure S7d-f). Interestingly, a complete Mn^{2+} replacement by Zn^{2+} is observed on the edge of plate-like Zn^{2+} -exchanged crystals, while away from the edges the Zn/Mn molar ratio is close to 1:2, indicating that Zn^{2+} ions enter from the edge of anionic slabs. The precise contents of metal ions in the pristine potassium compound and Zn^{2+} , Cd^{2+} , and Pb^{2+} -exchanged products were determined by ICP-AES (Table 3) and correspond well to the EDS analysis.

The PXRD patterns of the exchanged products confirm the topotactic character of the process and the formation of new isostructural compounds. A slight shift of the basal (002), (004), and (006) Bragg peaks to lower 2θ is observed in the patterns of Cs⁺ and Rb⁺ exchanged products suggesting a small expansion of the interlayer space compared to $K_x[Bi_{4-x}Mn_xS_6]$ (x=1.28) (Figure 6a). The c-axis lengths calculated by the position of (002) reflection follow the order: Cs⁺ (23.94 Å) > Rb⁺ (23.56 Å) > pristine (22.87 Å), which is consistent with the size of the intercalated cations. After Sr²⁺ exchange, the

three (00*l*) peaks broaden slightly and shift to lower 2θ , suggesting interlayer expansion (Figure 6b) and the insertion of hydrated species such as $Sr(H_2O)_6^{2+}$. For Zn^{2+} exchange, although its size (0.88 Å) is smaller than K^+ (1.52 Å), the positions of (00*l*) peaks do not shift appreciably after Zn^{2+} exchange, which also indicates the hydrated nature of intercalated Zn^{2+} . The heavily broadened Bragg peaks after Cr^{3+} , Pb^{2+} and Cd^{2+} exchange indicate a decrease of crystal size and increase in lattice disorder. The shift of the basal (00*l*) peaks to higher 2θ implies the contraction of the interlayer space caused by the smaller ionic sizes and strong covalent M-S bonding of the intercalated ions. This also indicates that these ions enter the structure in unhydrated form and are able to directly bind to the host layers.

The band gaps of Cs⁺ and Rb⁺ exchanged products are almost the same with that of the pristine suggesting a weak ionic interaction with the layers (Figure 6c). This is expected since the alkali ions do not contribute the energy levels of the CBM and VBM. The smaller band gaps of the Sr²⁺(1.26 eV), Zn²⁺(1.30 eV), Cd²⁺(1.26 eV), Pb²⁺(1.10 eV), and Cr³⁺(1.02 eV) exchanged products, however, indicate the stronger interaction between the intercalated ions and sulfur ligands in the slab in the form of direct M–S bonding (Figure 6d). Therefore, these ions significantly modify the electronic structure of the pristine material. These additional bonds can increase the electronic bandwidths as they tend to make the compounds more three-dimensional and lead to the narrower band gaps.

Work Functions. The work functions of $K_x[Bi_{4-x}Mn_xS_6]$ (x = 1.28) and Zn^{2+} , Cd^{2+} and Pb^{2+} exchanged products were measured using photoelectron spectroscopy in air to assess the energy levels of the VBM and CBM (Figure S8). Because the materials are semiconductors, these values are essentially the energy positions of the valence band maxima and are given in Table 3. Compared to $K_x[Bi_{4-x}Mn_xS_6]$ (x = 1.28), whose work function was measured at 5.26 eV, the work functions of Zn²⁺, Cd²⁺, and Pb²⁺-exchanged products increase to 5.80, 5.73, and 5.41 eV, respectively. Therefore, the new strong M-S bonds further stabilize the highest occupied states in the valence band as the weak K···S ionic interactions in the pristine material are replaced by stronger covalent bonding interactions between S²⁻ ions and these metal ions, which significantly modify the electronic structures. This is consistent with the drastic narrowing of the electronic bandgap described above.

Ion Exchange of Rb⁺, Cs⁺, and Zn²⁺ with $K_x[Bi_{4-x}Mn_xS_6]$ Single Crystals. Because the PXRD patterns reveal that the Rb⁺, Cs⁺, and Zn²⁺ exchanged products are highly crystalline, we were able to perform successful "single crystal to single crystal" ion-exchange reactions and precisely determine the structures of these products.

Diffraction-quality Rb⁺ and Cs⁺ exchanged crystals were picked out for detailed crystallographic analysis. The crystallographic data and details of the structure refinements are given in Table 4. The selected bond lengths and angles, atomic

Table 4. Crystallographic Data (180 K) and Details of the Structure Refinement of Rb⁺ and Cs⁺-Exchanged Single Crystals ^{a,b}

formula	$Rb_{0.88}Mn_{1.28}Bi_{2.72}S_{6} \\$	$Cs_{1.03}Mn_{1.28}Bi_{2.72}S_6$
space group	P6 ₃ /mmc	$P6_3/mmc$
$F_w(g \cdot \text{mol}^{-1})$	906.41	968.07
a (Å)	3.9529(2)	3.9548(2)
c (Å)	23.598(2)	24.099(2)
V (Å ³)	319.33(3)	326.42(3)
crystal color	black	black
$\rho_{\rm c}~({\rm g\cdot cm^{-3}})$	4.713	4.924
$\mu \left(\mathrm{mm}^{-1} \right)$	42.853	41.493
F(000)	386	410
data/parameters	143/16	204/16
$R_{ m int}$	0.0448	0.0507
$R1[I > 2\sigma(I)]$	0.0386	0.0337
wR_2 (all data)	0.0848	0.0833
GOF	1.319	1.274

^aR = Σ||F₀| - |F_c||/Σ|F₀|. ^bwR = Σ{[w(|F₀|² - |F_c|²)²]/Σ[w(|F₀|⁴)]}^{1/2} and $w = 1/[\sigma^2(F_0^2) + (0.0117P)^2 + 20.416P]$ for Rb_{0.88}Mn_{1.28}Bi_{2.72}S₆ and $w = 1/[\sigma^2(F_0^2) + (0.0426P)^2 + 4.7319P]$ for Cs_{1.03}Mn_{1.28}Bi_{2.72}S₆ where $P = (F_0^2 + 2F_c^2)/3$

coordinates, and anisotropic displacement parameters are given in Tables S3–S8. X-ray diffraction refinement reveals that the exchanged products are isostructural with the pristine potassium compound. The representation of crystal structures of $K_x [Bi_{4-x}Mn_xS_6]$ and its Rb^+ and Cs^+ -exchanged analogues are shown in Figure S9, along with the interlayer distances and Mn/Bi–S bond lengths. The interlayer space extends from 5.19 to 5.40 Å and 5.67 Å after Rb^+ and Cs^+ exchange, respectively, while the Mn/Bi–S bond lengths remain almost the same (Figure S9e–g). The refinement gave the formulas $Rb_{0.88}Mn_{1.28}Bi_{2.72}S_6$ and $Cs_{1.03}Mn_{1.28}Bi_{2.72}S_6$, which are somewhat lower in alkali metal content. EDS analysis of the ion-

exchange products also show lower Rb/Mn (0.69) and Cs/Mn (0.81) ratios (Figure S7a,b), compared with the K/Mn ratio 1:1 in the pristine compound. On the basis of charge balanced arguments these formulas indicate that the average Mn oxidation states in the Rb⁺ and Cs⁺-exchanged products have changed from +2 to +2.31 and +2.2, respectively. The XPS spectrum of the pristine compound $K_x[Bi_{4-x}Mn_xS_6]$ (x = 1.28), the peak fitted as 639.6 and 640.9 eV can be assigned to Mn²⁺ 2 $p_{3/2}$, while the peak at 644.8 eV is Mn(II) satellite, Figure 7. This result is consistent with the reported data of

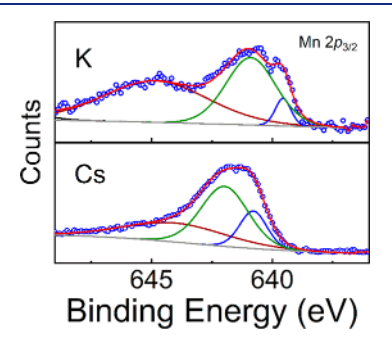


Figure 7. Mn $2p_{3/2}$ peaks in the XPS spectrum of $K_x[Bi_{4-x}Mn_xS_6]$ (x = 1.28) and Cs^{+} -exchanged product.

the binding energy of $\rm Mn^{2+}$ in $\rm MnS^{20,56}$ and indicates a $\rm Mn^{2+}$ oxidation state. After $\rm Cs^+$ exchange, however, the peaks of Mn $\rm 2p_{3/2}$ shift to higher binding energy (640.8 and 641.9 eV) indicating the oxidation of $\rm Mn^{2+}$. The Mn $\rm 2p_{3/2}$ peak at 641.9 eV is assigned to $\rm Mn^{3+}$. The strongly electropositive nature of $\rm Cs^+$ makes the $\rm [Bi_{2.72}Mn_{1.28}S_6]^{1.28-}$ slabs more negatively charged which is relieved by the higher oxidation state of Mn as has been previously explained for KMS-1. 20

Compared with monovalent alkali ion exchange, the bivalent ion exchange especially with soft metal ions that can strongly bind to the [Bi_{2.72}Mn_{1.28}S₆]^{1.28-} layers, causes serious lattice disorder which leads to poor crystal quality. However, in the case of Zn^{2+} exchange, the ions exists as $[Zn(H_2O)_6]^{2+}$ and the product exhibits good crystallization allowing for diffractionquality crystals to be selected. EDS analysis of the Zn²⁺exchanged single crystal reveals that most Mn2+ ions are not replaced by Zn2+ ions. The crystallographic data and details of the structure refinements are given in Table S9. The selected bond lengths and angles, atomic coordinates, and anisotropic displacement parameters are given in Tables S10-S12. The crystal possessed good crystallinity after Zn2+ exchange, and our refinement resulted in good residual factors (R1 = 0.0326and wR2 = 0.0772) and goodness of fit (S = 1.392). The electron density peaks at 2b and 2d sites between the layers were labeled as Zn1 and Zn2 with occupancies of 19% and 13%, respectively (Figure S9d). The interlayer space extends from 5.19 to 5.34 Å after Zn²⁺ exchange, which indicates the hydrated nature of intercalated Zn²⁺ ions. The Mn/Bi-S bond lengths remain almost unchanged after Zn²⁺ exchange (Figure S9h).

Isotherm and Kinetic Studies of Cs⁺, Cd²⁺, and Pb²⁺ Ion Exchange. The adsorption performance of $K_x[Bi_{4-x}Mn_xS_6]$ (x = 1.28) toward heavy metal ions was assessed with detailed studies using the so-called batch method. Specifically, we performed isotherm, kinetics, competitive, and pH-dependent ion exchange reactions of Cs⁺, Cd²⁺, and Pb²⁺ ions.

Cd²⁺, Pb²⁺. The ion-exchange studies of Cd²⁺ and Pb²⁺ were performed using the batch method (V:m=1000:1 mL/g, pH ≈ 5.5 for Cd²⁺, 5.0 for Pb²⁺, room temperature). The Cd²⁺, Pb²⁺ sorption isotherm curves are graphed in Figure 8a and 8b.

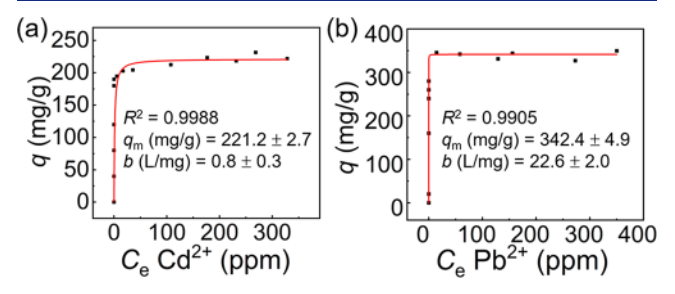


Figure 8. Sorption isotherm data for (a) Cd^{2+} and (b) Pb^{2+} ion exchange. The red lines represent the fitting of the data with the Langmuir model (fitting data for Cd^{2+} : $q_m = 221(3)$ mg/g, b = 0.8(0.3) L/mg; fitting data for Pb^{2+} : $q_m = 342(5)$ mg/g, b = 23(2) L/mg).

Excellent fits of the curves (correlation coefficient $R^2 > 99\%$) were obtained with the Langmuir isotherm model (1) expressed as follows:

$$q = q_{\rm m} \frac{bC_{\rm e}}{1 + bC_{\rm e}} \tag{1}$$

where q (mg/g) is the sorption amount at the equilibrium concentration $C_{\rm e}$ (ppm), $q_{\rm m}$ is the maximum sorption capacity, and b is a constant. The maximum Cd²⁺ and Pb²⁺ sorption capacities calculated by the Langmuir model are 221(3) mg/g and 342(5) mg/g, respectively. The Cd²⁺ sorption capacity matches well with the theoretical maximum capacity (245 mg/g) with the exchanged product formula Cd_{1.91}Bi_{2.72}S₆ obtained by ICP-AES analysis. The Pb²⁺ sorption capacity is also close to the theoretical maximum capacity (360 mg/g) with the exchanged product formula Pb_{1.52}Mn_{0.20}Bi_{2.72}S₆. The distribution coefficient $K_{\rm d}$ (2) expressed as follows:

$$K_{\rm d} = \left(\frac{V}{m}\right) \frac{(C_0 - C_{\rm e})}{C_{\rm e}} \tag{2}$$

is an indicator of the sorption capacity and selectivity of a material, where C_0 (ppm) is the initial concentration. The K_d of Cd^{2+} and Pb^{2+} were found to be greater than 10^7mL/g with low initial concentrations (Figure S10). The adsorption capacities of $K_x[Bi_{4-x}Mn_xS_6]$ (x=1.28) toward Cd^{2+} and Pb^{2+} are comparable for those of the leading absorbents listed in Table S13. Especially, $K_x[Bi_{4-x}Mn_xS_6]$ possesses particularly

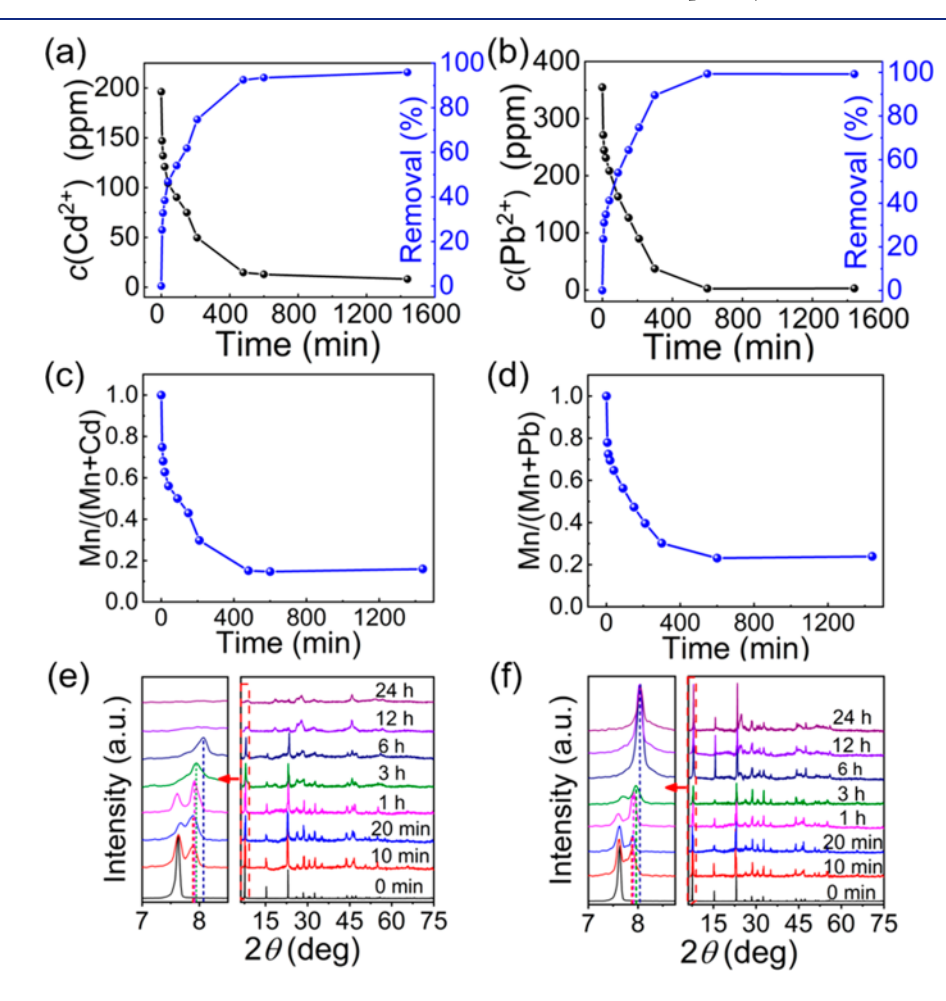


Figure 9. Kinetics curve and removal of (a) Cd^{2+} and (b) Pb^{2+} . (Initial concentration: Cd^{2+} 200 ppm, Pb^{2+} : 350 ppm). The time-dependent molar ratios of (c) Mn/(Mn + Cd) and (d) Mn/(Mn + Pb) in the exchanged products determined by ICP-AES. PXRD patterns of (e) Cd^{2+} and (f) Pb^{2+} exchanged products with different exchange times.

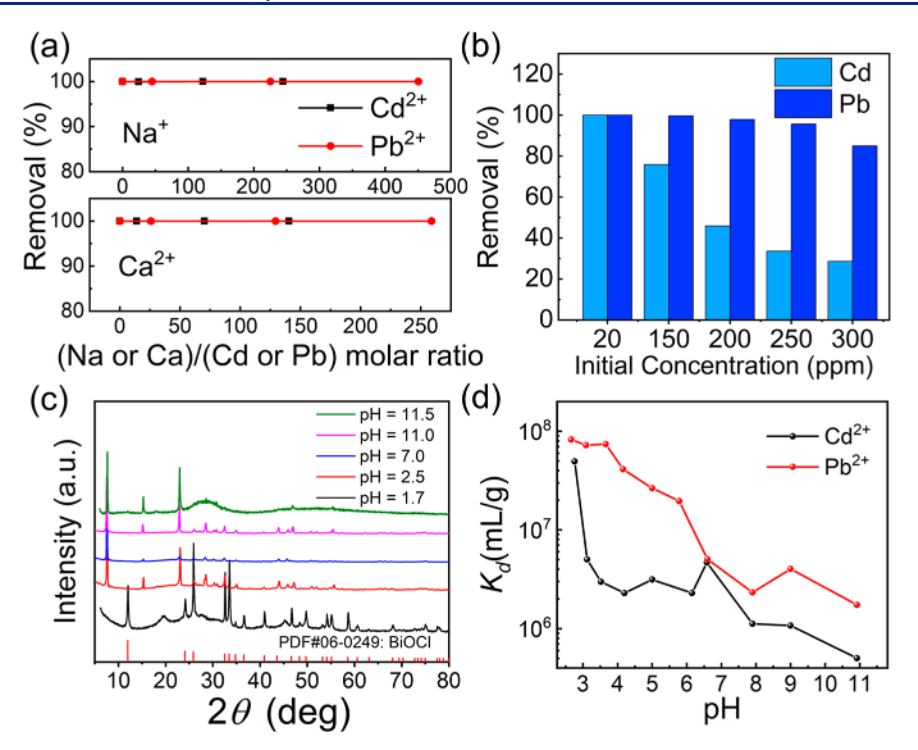


Figure 10. (a) Removal of Cd^{2+} and Pb^{2+} in various concentration solution of Na^+ or Ca^{2+} , initial Cd^{2+} and Pb^{2+} concentrations: 6 ppm. (b) Competitive ion-exchange capacities for Cd^{2+} and Pb^{2+} for various concentrations. (c) PXRD patterns of $K_x[Bi_{4-x}Mn_xS_6]$ (x=1.28) in pH range 1.7–11.5. (d) K_d of Cd^{2+} and Pb^{2+} exchange at the pH range of 2.7–11.0 with initial concentration of 20 ppm.

high K_d among these adsorbents, indicating tremendous affinity of this material for Cd^{2+} and Pb^{2+} .

The kinetics of Cd²⁺ and Pb²⁺ ion exchange were studied with the initial concentration of 200 ppm for Cd²⁺ and 350 ppm for Pb²⁺. In both cases equilibrium was reached within 10 h, and the removal rates were >96% and >99%, respectively (Figure 9a and b). We also monitored the release rates of K⁺ and Mn²⁺ during the exchange (Figure S11). The results reveal that the K⁺ ions in the interlayer space exchanged faster than the Mn^{2+} ions in the slabs as expected. The plots of Mn/(Mn +M) (M = Cd, Pb) (Figure 9c and d) based on elemental analysis acquired using ICP-AES show decreasing fraction of Mn in the ion exchange products. The process can be monitored by PXRD, as shown in Figure 9e and f. In both reactions, a new Bragg peak with higher 2θ value than that of the original basal (002) peak appears within 10 min, indicating the fast intercalation dynamics of Cd^{2+} or Pb^{2+} ions. As the ion exchange proceeds, the new Bragg peak shifts to higher 2θ position, as the original basal (002) peak diminishes. Further Cd²⁺ exchange (>6 h) causes poor crystallinity of the products as revealed by the extensive broadening of Bragg peaks. In comparison, the Pb²⁺-exchanged product retains the structural features of the pristine compound with broader but still strong Bragg peaks after 24 h exchange.

Cs⁺. Because of the change in the Mn²⁺ oxidation in the Cs⁺ exchange process (which uses atmospheric oxygen as the oxidant), isotherm and kinetic studies were carried out in both air and in Ar atmosphere. The Cs⁺ sorption capacities in Ar are higher than those in air, Figure S12. The difference in capacities results from the Mn²⁺ oxidation by O₂ in air which reduces the demand of Cs⁺ to balance charge. An interesting adsorption and release behavior was observed when we conducted the kinetic study in air, which indicates that the dynamics of Mn²⁺ oxidation in $K_x[Bi_{4-x}Mn_xS_6]$ (x = 1.28) is

slower than that in KMS-1. Detailed discussion about the Cs⁺ exchange is given in the SI.

Competitive and pH-Dependent lon Exchange Experiments. The competitive sorption of Cs^+ in concentrated solutions of Na^+ or Ca^{2+} was studied under Ar gas. The removal of Cs^+ decreased slightly in the presence of 5–30 fold excess of Na^+ , but dropped to 50% in the presence of 17-fold excess of Ca^{2+} , see Figure S13. Thus, Ca^{2+} is a stronger competitor than Na^+ for Cs^+ exchange and can be rationalized by the double positive charge of this ion. We also checked the ability to remove Cd^{2+} and Pb^{2+} from solutions containing a high excess of Na^+ or Ca^{2+} . The high concentration of Na^+ or Ca^{2+} did not affect the absorption toward these heavy metal ions. Remarkably, the Cd^{2+} and Pb^{2+} concentrations can be reduced below 1 ppb (V:m=1000 mL/g, initial concentration: 6 ppm) with the existence of high concentration of Na^+ and Ca^{2+} , see Figure 10a.

To check the relative selectivity of $K_x[Bi_{4-x}Mn_xS_o]$ (x=1.28) toward Cd^{2+} and Pb^{2+} , competitive ion-exchange (containing both ions) were performed with solutions containing 20, 150, 200, 250, 300 ppm of each ion, Figure 10b. At the very large concentration of 300 ppm the Pb^{2+} removal is around 85.0% and increases to 99.6% at 150 ppm. In comparison, the Cd^{2+} removal is only 28.6% at 300 ppm, and it increases to 75.9% at 150 ppm. Both Pb^{2+} and Cd^{2+} removal rates can exceeded 99.9% at 20 ppm. The competitive experiments clearly indicate that the material prefers Pb^{2+} over Cd^{2+} which is opposite to the trend observed in KMS-1.

The acid and base stability of $K_x[Bi_{4-x}Mn_xS_6]$ (x = 1.28)was investigated in a wide range of pH values (1.7–11.5). The compound retained the layered structure and high crystallinity in pH between 2.5 and 11.0 after stirring for 2 days (Figure 10c). Higher concentration of hydrochloric acid (pH< 2.5) can react with $K_x[Bi_{4-x}Mn_xS_6]$ (x = 1.28) to produce BiOCl-

(PDF#06-0249). At pH = 11.5, some unidentified phases with low K content and high O content were observed by SEM and EDS analysis (Figure S14). Cs⁺ exchange experiments of $K_x[Bi_{4-x}Mn_xS_6]$ in solutions of various pH (2.6–11) were conducted in Ar gas with initial Cs⁺ concentration of 10 ppm (Figure S15). The results indicated that $K_x[Bi_{4-x}Mn_xS_6]$ can remove over 80% of Cs⁺ in the pH range of 3.6–11. Even at pH = 2.6 the removal of Cs^+ still retains near 70%. This remarkable capture of Cs⁺ in acidic conditions should origin from the relatively "softer" nature of Cs⁺ ion compared with the hard proton ion. The effect of pH on the Cd²⁺ and Pb²⁺ exchange was also studied in the range of 2.7-11.0 with initial concentration of 20 ppm (Figure 10d). $K_x[Bi_{4-x}Mn_xS_6]$ (x =1.28) displays a maximum $K_{\rm d}$ (~2.1 × 10⁷ mL/g) for Cd²⁺ at pH \approx 2.7, while $K_{\rm d}$ values at pH > 3.1 are all in the range of 5.0 \times 10⁵–5.0 \times 10⁶ mL/g. The $K_{\rm d}$ The Pb²⁺ uptake increases in lower pH with the maximum $K_d = 8.3 \times 10^7$ at pH = 2.7. Pb²⁺ $K_{\rm d}$ values at pH 3.1-6.6 are all in the range of 2.0-7.4 × 10⁷ mL/g, while the K_d values decrease to $1.7-5.0 \times 10^6$ mL/g at higher pH (>6.6). Such high K_d values validate the strong uptake of $K_r[Bi_{4-r}Mn_rS_6]$ (x = 1.28) toward Cd^{2+} and Pb^{2+} in the pH range tested.

CONCLUSIONS

 $K_x[Bi_{4-x}Mn_xS_6]$ (x = 1.28) was designed to possess powerful ion-exchange properties starting from the Bi₂Se₃-type layer and making it anionic via the replacement of some Bi³⁺ atoms with Mn²⁺ atoms. However, the material possesses dual characteristics as the paramagnetic compound exhibits interesting semiconducting characteristics with a direct band gap of 1.40 eV and low effective carrier masses. Topotactic ion exchange can be performed rapidly by $K_x[Bi_{4-x}Mn_xS_6]$ (x = 1.28) with a variety of ions such as Rb+, Cs+, Sr2+, Pb2+, Cd2+, Cr3+, and Zn²⁺. The structures of Rb⁺, and Cs⁺ exchanged crystals were solved by single-crystal X-ray diffraction and confirmed an unusual topotactic oxidation of Mn2+ after Rb+ and Cs+ exchange in air. The formation of Mn³⁺ lowers the absorption capacity for Rb⁺ and Cs⁺ but facilitates the kinetics of their subsequent release. The $K_x[Bi_{4-x}Mn_xS_6]$ (x = 1.28) systemexhibits efficient adsorption of Cd2+ and Pb2+ with high exchange capacities of 221.2 and 342.4 mg/g and particularly high K_d of 10^7mL/g , and can efficiently remove these ions in a wide pH range (2.5-11.0) and with competitive cations present in large excess. All of these highlight the $K_x[Bi_{4-x}Mn_xS_6]$ (x = 1.28) as a highly selective adsorbent for the quantitative removal of heavy metals and radioactive ions from industrial and nuclear waste waters. Finally, the ion exchange reactions of $K_x[Bi_{4-x}Mn_xS_6]$ are a gateway to new materials of the type $M_x[Bi_{4-x}Mn_xS_6]$ with kinetic control as afforded by the low temperatures.

ASSOCIATED CONTENT

S Supporting Information

The Supporting Information is available free of charge on the ACS Publications website at DOI: 10.1021/jacs.9b08674.

Experimental section of XRD, SEM, UV-vis, DSC, and XPS; results and discussion about Cs⁺ adsorption; figures of SEM, EDS, electronic structures, electrical conductivity, and work functions; and tables of atomic coordinates and displacement parameters (PDF)

X-ray crystallographic information (CIF)

X-ray crystallographic information (CIF)

X-ray crystallographic information (CIF) X-ray crystallographic information (CIF)

AUTHOR INFORMATION

Corresponding Authors

*huangfq@pku.edu.cn

*m-kanatzidis@northwestenrn.edu

ORCID 🧐

Haijie Chen: 0000-0003-3567-1763 Ido Hadar: 0000-0003-0576-9321 Xian Zhang: 0000-0003-0681-8201

Mercouri G. Kanatzidis: 0000-0003-2037-4168

Notes

The authors declare no competing financial interest.

ACKNOWLEDGMENTS

Work at Northwestern was supported partly by the National Science Foundation (Grant DMR-1708254). This work also was partially supported by the Innovation Program of the CAS (Grant KJCX2-EW-W11), "Strategic Priority Research Program (B)" of the Chinese Academy of Sciences (Grants XDB04040200), NSF of China (Grants 91122034, 51125006, 51202279, 61376056, and 21201012), and Science and Technology Commission of Shanghai (Grant 12XD1406800). PYSA measurements were carried out with equipment acquired by ONR DURIP grant N00014-18-1-2102.

REFERENCES

- (1) Shannon, M. A.; Bohn, P. W.; Elimelech, M.; Georgiadis, J. G.; Mariñas, B. J.; Mayes, A. M. Science and technology for water purification in the coming decades. *Nature* **2008**, 452, 301–311.
- (2) Schwarzenbach, R. P.; Escher, B. I.; Fenner, K.; Hofstetter, T. B.; Johnson, C. A.; Von Gunten, U.; Wehrli, B. The challenge of micropollutants in aquatic systems. *Science* **2006**, *313*, 1072–1077.
- (3) Sharma, S. K. Heavy Metals in Water: Presence, Removal and Safety; RSC: 2014.
- (4) Sarkar, B. Heavy Metals in the Environment; CRC Press: 2002.
- (5) Naja, G. M.; Volesky, B. Toxicity and sources of Pb, Cd, Hg, Cr, As, and radionuclides in the environment. *Heavy Metals in the Environment* **2009**, *8*, 16–18.
- (6) Sarı, A.; Tuzen, M.; Citak, D.; Soylak, M. Equilibrium, kinetic and thermodynamic studies of adsorption of Pb (II) from aqueous solution onto Turkish kaolinite clay. *J. Hazard. Mater.* **2007**, *149*, 283–291.
- (7) Sarı, A.; Tuzen, M.; Soylak, M. Adsorption of Pb (II) and Cr (III) from aqueous solution on Celtek clay. *J. Hazard. Mater.* **2007**, 144, 41–46.
- (8) Benhammou, A.; Yaacoubi, A.; Nibou, L.; Tanouti, B. Adsorption of metal ions onto Moroccan stevensite: kinetic and isotherm studies. *J. Colloid Interface Sci.* **2005**, 282, 320–326.
- (9) Bansal, R. C.; Goyal, M. Activated carbon adsorption. CRC press: 2005.
- (10) Manos, M. J.; Kanatzidis, M. G. Metal sulfide ion exchangers: superior sorbents for the capture of toxic and nuclear waste-related metal ions. *Chem. Sci.* **2016**, *7*, 4804–4824.
- (11) He, W.; Ai, K.; Ren, X.; Wang, S.; Lu, L. Inorganic layered ion-exchangers for decontamination of toxic metal ions in aquatic systems. *J. Mater. Chem. A* **2017**, *5*, 19593–19606.
- (12) Barakat, M. New trends in removing heavy metals from industrial wastewater. *Arabian J. Chem.* **2011**, *4*, 361–377.
- (13) Fan, Q.; Li, Z.; Zhao, H.; Jia, Z.; Xu, J.; Wu, W. Adsorption of Pb (II) on palygorskite from aqueous solution: effects of pH, ionic strength and temperature. *Appl. Clay Sci.* **2009**, *45*, 111–116.

- (14) Fu, F.; Wang, Q. Removal of heavy metal ions from wastewaters: a review. *J. Environ. Manage.* **2011**, 92, 407–418.
- (15) Hui, K.; Chao, C. Y. H.; Kot, S. Removal of mixed heavy metal ions in wastewater by zeolite 4A and residual products from recycled coal fly ash. *J. Hazard. Mater.* **2005**, *127*, 89–101.
- (16) Jiang, M. Q.; Jin, X. Y.; Lu, X. Q.; Chen, Z. L. Adsorption of Pb (II), Cd (II), Ni (II) and Cu (II) onto natural kaolinite clay. *Desalination* **2010**, 252, 33–39.
- (17) Kobya, M.; Demirbas, E.; Senturk, E.; Ince, M. Adsorption of heavy metal ions from aqueous solutions by activated carbon prepared from apricot stone. *Bioresour. Technol.* **2005**, *96*, 1518–1521.
- (18) Ozdes, D.; Duran, C.; Senturk, H. B. Adsorptive removal of Cd (II) and Pb (II) ions from aqueous solutions by using Turkish illitic clay. *J. Environ. Manage.* **2011**, *92*, 3082–3090.
- (19) Manos, M. J.; Ding, N.; Kanatzidis, M. G. Layered metal sulfides: exceptionally selective agents for radioactive strontium removal. *Proc. Natl. Acad. Sci. U. S. A.* **2008**, 105, 3696–3699.
- (20) Manos, M. J.; Kanatzidis, M. G. Highly Efficient and Rapid Cs^+ Uptake by the Layered Metal Sulfide $K_{2x}Mn_xSn_{3-x}S_6$ (KMS-1). *J. Am. Chem. Soc.* **2009**, *131*, 6599–6607.
- (21) Manos, M. J.; Kanatzidis, M. G. Sequestration of heavy metals from water with layered metal sulfides. *Chem. Eur. J.* **2009**, *15*, 4779–4784.
- (22) Manos, M. J.; Petkov, V. G.; Kanatzidis, M. G. $H_{2x}Mn_xSn_{3-x}S_6$ (x = 0.11-0.25): A Novel Reusable Sorbent for Highly Specific Mercury Capture Under Extreme pH Conditions. *Adv. Funct. Mater.* **2009**, *19*, 1087–1092.
- (23) Manos, M. J.; Kanatzidis, M. G. Layered metal sulfides capture uranium from seawater. *J. Am. Chem. Soc.* **2012**, *134*, 16441–16446. (24) Mertz, J. L.; Fard, Z. H.; Malliakas, C. D.; Manos, M. J.; Kanatzidis, M. G. Selective Removal of Cs^+ , Sr^{2+} , and Ni^{2+} by $K_{2x}Mg_xSn_{3-x}S_6$ (x=0.5-1)(KMS-2) Relevant to Nuclear Waste Remediation. *Chem. Mater.* **2013**, *25*, 2116–2127.
- (25) Feng, M. L.; Sarma, D.; Qi, X. H.; Du, K. Z.; Huang, X. Y.; Kanatzidis, M. G. Efficient removal and recovery of uranium by a layered organic-inorganic hybrid thiostannate. *J. Am. Chem. Soc.* **2016**, 138, 12578–12585.
- (26) Li, J. R.; Wang, X.; Yuan, B.; Fu, M. L.; Cui, H. J. Robust removal of heavy metals from water by intercalation chalcogenide [CH₃NH₃]_{2x}Mn_xSn_{3-x}S₆·0.5H₂O. *Appl. Surf. Sci.* **2014**, 320, 112–119.
- (27) Hassanzadeh Fard, Z.; Malliakas, C. D.; Mertz, J. L.; Kanatzidis, M. G. Direct extraction of Ag⁺ and Hg²⁺ from cyanide complexes and mode of binding by the layered K₂MgSn₂S₆ (KMS-2). *Chem. Mater.* **2015**, *27*, 1925–1928.
- (28) Neeway, J. J.; Asmussen, R. M.; Lawter, A. R.; Bowden, M. E.; Lukens, W. W.; Sarma, D.; Riley, B. J.; Kanatzidis, M. G.; Qafoku, N. P. Removal of TcO₄⁻ from representative nuclear waste streams with layered potassium metal sulfide materials. *Chem. Mater.* **2016**, 28, 3976–3983.
- (29) Xiao, C.; Hassanzadeh Fard, Z.; Sarma, D.; Song, T. B.; Xu, C.; Kanatzidis, M. G. Highly efficient separation of trivalent minor actinides by a layered metal sulfide (KInSn₂S₆) from acidic radioactive waste. *J. Am. Chem. Soc.* **2017**, *139*, 16494–16497.
- (30) Li, J. R.; Xu, L.; Fu, M. L.; Wang, Y. X.; Xiao, H. Towards magnetic responsive chalcogenides for efficient separation in water treatment: facile synthesis of magnetically layered chalcogenide Fe₃O₄/KMS-1 composite adsorbents and their zinc removal application in water. *Inorg. Chem. Front.* **2018**, *5*, 403–412.
- (31) Qi, X. H.; Du, K. Z.; Feng, M. L.; Li, J. R.; Du, C. F.; Zhang, B.; Huang, X. Y. A two-dimensionally microporous thiostannate with superior Cs⁺ and Sr²⁺ ion-exchange property. *J. Mater. Chem. A* **2015**, 3, 5665–5673.
- (32) Qi, X. H.; Du, K. Z.; Feng, M. L.; Gao, Y. J.; Huang, X. Y.; Kanatzidis, M. G. Layered $A_2Sn_3S_7\cdot 1.25H_2O$ (A= Organic Cation) as Efficient Ion-Exchanger for Rare Earth Element Recovery. J. Am. Chem. Soc. **2017**, 139, 4314–4317.
- (33) Sarma, D.; Islam, S. M.; Subrahmanyam, K.; Kanatzidis, M. G. Efficient and selective heavy metal sequestration from water by using

- layered sulfide $K_{2x}Sn_{4-x}S_{8-x}$ (x = 0.65-1; KTS-3). J. Mater. Chem. A **2016**, 4, 16597–16605.
- (34) Rathore, E.; Pal, P.; Biswas, K. Layered Metal Chalcophosphate (K-MPS-1) for Efficient, Selective, and ppb Level Sequestration of Pb from Water. *J. Phys. Chem. C* **2017**, *121*, 7959–7966.
- (35) Rathore, E.; Pal, P.; Biswas, K. Reversible and Efficient Sequestration of Cesium from Water by the Layered Metal Thiophosphate K_{0.48}Mn_{0.76}PS₃·H₂O. *Chem. Eur. J.* **2017**, 23, 11085–11092.
- (36) Gash, A. E.; Spain, A. L.; Dysleski, L. M.; Flaschenriem, C. J.; Kalaveshi, A.; Dorhout, P. K.; Strauss, S. H. Efficient recovery of elemental mercury from Hg (II)-contaminated aqueous media using a redox-recyclable ion-exchange material. *Environ. Sci. Technol.* **1998**, 32, 1007–1012.
- (37) Schöllhorn, R.; Roer, W.; Wagner, K. Topotactic formation and exchange reactions of hydrated layered tin sulfides $A_x(H_2O)_y SnS_2$. *Monatsh. Chem.* **1979**, *110*, 1147–1152.
- (38) Ai, K.; Ruan, C.; Shen, M.; Lu, L. MoS₂ nanosheets with widened interlayer spacing for high efficiency removal of mercury in aquatic systems. *Adv. Funct. Mater.* **2016**, *26*, 5542–5549.
- (39) Zhao, J.; Islam, S. M.; Kontsevoi, O. Y.; Tan, G.; Stoumpos, C. C.; Chen, H.; Li, R.; Kanatzidis, M. G. The Two-Dimensional A_x Cd $_x$ Bi $_{4-x}$ Q $_6$ (A=K, Rb, Cs; Q = S, Se): Direct Bandgap Semiconductors and Ion-Exchange Materials. *J. Am. Chem. Soc.* **2017**, 139, 6978–6987.
- (40) Zhao, J.; Islam, S. M.; Hao, S.; Tan, G.; Stoumpos, C. C.; Wolverton, C.; Chen, H.; Luo, Z.; Li, R.; Kanatzidis, M. G. Homologous Series of 2D Chalcogenides Cs-Ag-Bi-Q (Q = S, Se) with Ion-Exchange Properties. *J. Am. Chem. Soc.* **2017**, *139*, 12601–12609.
- (41) Ikeue, K.; Shiiba, S.; Machida, M. Novel visible-light-driven photocatalyst based on Mn–Cd–S for efficient H₂ evolution. *Chem. Mater.* **2010**, 22, 743–745.
- (42) Liu, L.; Qi, Y.; Lu, J.; Lin, S.; An, W.; Liang, Y.; Cui, W. A stable Ag₃PO₄@ g-C₃N₄ hybrid core@ shell composite with enhanced visible light photocatalytic degradation. *Appl. Catal., B* **2016**, *183*, 133–141.
- (43) Shao, H. F.; Zhang, Y. B.; Qian, X. F.; Yin, J.; Zhu, Z. K. Preparation of rod-shape PbSO₄ nanocrystal and its phase transition to PbS. *Mater. Lett.* **2005**, *59*, 3507–3513.
- (44) Chondroudis, K.; Hanko, J. A.; Kanatzidis, M. G. Chemistry of Gold in Molten Alkali Metal Polychalcophosphate Fluxes. Synthesis and Characterization of the Low-Dimensional Compounds A_3 AuP₂Se₈ (A = K, Rb, Cs), A_2 Au₂P₂Se₆ (A = K, Rb), A_2 AuPS₄ (A = K, Rb, Cs), and AAuP₂S₇ (A = K, Rb). *Inorg. Chem.* **1997**, 36, 2623–2632.
- (45) Hanko, J. A.; Sayettat, J.; Jobic, S.; Brec, R.; Kanatzidis, M. G. $A_2\text{CuP}_3S_9$ (A = K, Rb), $Cs_2\text{Cu}_2P_2S_6$, and $K_3\text{CuP}_2S_7$: New phases from the dissolution of copper in molten polythiophosphate fluxes. *Chem. Mater.* **1998**, *10*, 3040–3049.
- (46) Sheldrick, G. SHELX-97, program for the solution and refinement of crystal structures; University of Göttingen, Germany, 1997.
- (47) Baikie, I. D.; Grain, A.; Sutherland, J.; Law, J. Near ambient pressure photoemission spectroscopy of metal and semiconductor surfaces. *Phys. Status Solidi-C* **2015**, *12*, 259–262.
- (48) Blöchl, P. E. Projector augmented-wave method. Phys. Rev. B: Condens. Matter Mater. Phys. 1994, 50, 17953.
- (49) Kresse, G.; Hafner, J. Ab initio molecular dynamics for liquid metals. *Phys. Rev. B: Condens. Matter Mater. Phys.* **1993**, 47, 558.
- (50) Kresse, G.; Furthmüller, J. Efficiency of ab-initio total energy calculations for metals and semiconductors using a plane-wave basis set. *Comput. Mater. Sci.* **1996**, *6*, 15–50.
- (51) Kresse, G.; Furthmüller, J. Efficient iterative schemes for ab initio total-energy calculations using a plane-wave basis set. *Phys. Rev. B: Condens. Matter Mater. Phys.* **1996**, *54*, 11169.
- (52) Perdew, J. P.; Burke, K.; Ernzerhof, M. Generalized gradient approximation made simple. *Phys. Rev. Lett.* **1996**, *77*, 3865.
- (53) Mott, N. F.; Davis, E. A. Electronic Processes in Non-Crystalline Materials; OUP Oxford: 2012.

- (54) Mott, N. Conduction in glasses containing transition metal ions. J. Non-Cryst. Solids 1968, 1, 1–17.
- (55) Ilton, E. S.; Post, J. E.; Heaney, P. J.; Ling, F. T.; Kerisit, S. N. XPS determination of Mn oxidation states in Mn (hydr) oxides. *Appl. Surf. Sci.* **2016**, *366*, 475–485.
- (56) Strohmeier, B. R.; Hercules, D. M. Surface spectroscopic characterization of manganese/aluminum oxide catalysts. *J. Phys. Chem.* **1984**, *88*, 4922–4929.